ACS Partner Journal

Journal of the American Society for Mass Spectrometry

pubs.acs.org/jasms

Article

Improvement of Lipid Detection in Mouse Brain and Human Uterine Tissue Sections Using In Situ Matrix Enhanced Secondary Ion Mass Spectrometry

Thomas Daphnis, Benjamin Tomasetti, Vincent Delmez, Kevin Vanvarenberg, Véronique Préat, Charlotte Thieffry, Patrick Henriet, Christine Dupont-Gillain, and Arnaud Delcorte*

Cite This: https://doi.org/10.1021/jasms.3c00195

Read Online

ACCESS | Metrics & More | Article Recommendations | Supporting Information

ABSTRACT: The potential of mass spectrometry imaging, and especially ToF-SIMS 2D and 3D imaging, for submicrometer-scale, label-free molecular localization in biological tissues is undisputable. Nevertheless, sensitivity issues remain, especially when one wants to achieve the best lateral and vertical (nanometer-scale) resolution. In this study, the interest of in situ matrix transfer for tissue analysis with cluster ion beams (Bi_n^+, Ar_n^+) is explored in detail, using a series of six low molecular weight acidic (MALDI) matrices. After estimating the sensitivity enhancements for phosphatidylcholine (PC), an abundant lipid type present in almost any kind of cell membrane, the most promising matrices were softly transferred in situ on mouse brain and human uterine tissue samples using a 10 keV Ar_{3000}^+ cluster beam. Signal enhancements up to 1 order of magnitude for intact lipid signals were observed in both tissues under Bi_5^+ and Ar_{3000}^+ bombardment. The main findings of this study lie in the in-depth characterization of uterine tissue samples, the demonstration that the transferred matrices also improve signal efficiency in the negative ion polarity and that they perform as well when using Bi_n^+ and Ar_n^+ primary ions for analysis and imaging.

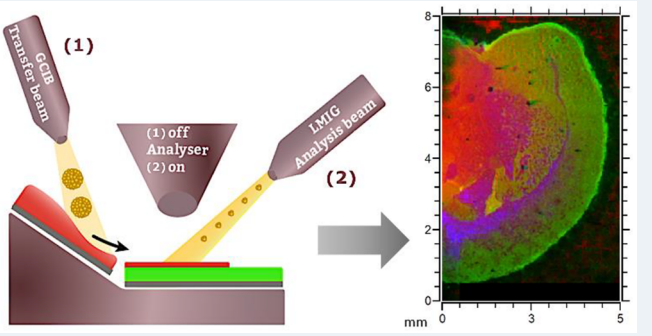

1. INTRODUCTION

During the past decade, mass spectrometry imaging (MSI) has gained substantial momentum due to its remarkable ability to provide valuable insights into cell/tissue molecular organization.[1,2] Indeed, this label-free multiplexed imaging technique is able to detect a wide variety of biomolecules ranging from small metabolites,[3] drugs and xenobiotics,[4] lipids,[5] sugars,[6] to proteins,[7] etc. without prior targeting. MSI has now been applied to a wide range of tissues/organs such as rodent brains which became the gold standard to test new MSI methodologies[8−11] or more exotic ones like mummies.[12] MSI allows researchers to, among others, detect diseases,[13] study the intracellular localization of drugs,[14] and obtain a better understanding of tissue metabolomics.[15] In turn, MSI finds applications in the biological and pharmaceutical fields, as well as many others. For instance, several diseases such as Alzheimer's disease[13] or breast cancer[16] were shown to affect the lipidic cell membrane composition. It is therefore particularly useful for disease detection and understanding to be able to have a microscopic look at these lipid membranes. MSI makes such investigations possible, while the application of classical label-based imaging techniques to lipids is questionable considering their small mass.[17]

A number of MS techniques have proven their capability to provide useful information like matrix-assisted laser desorption ionization (MALDI) MS,[18−20] desorption electrospray ionization (DESI) MS,[21−24] and secondary ion mass spectrometry (SIMS).[2,5,8,13] SIMS, the oldest of these methods, uses focused kiloelectronvolt ion beams to sputter or desorb neutral and charged molecular material from the top nanometers of the surface. Recent developments in SIMS, such as the introduction of gas cluster ion beams (GCIB),[25] the improvement of mass analyzer performance[9] and the evolution of organic sample preparation procedures[26,27] unleashed a renewed interest for this technique in the MSI community. The main advantage of SIMS compared to other MSI techniques is its ability to reach high spatial resolution, down to 100 nm laterally in the best-case scenario, using liquid metal ion sources such as Bi_{3-5}^+, and a few nm in depth.[28] Moreover,

Received: May 23, 2023
Revised: August 11, 2023
Accepted: September 1, 2023

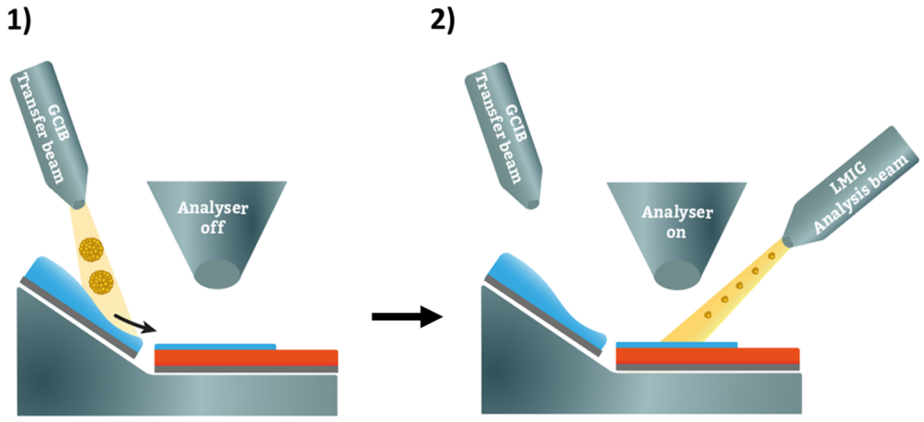

Figure 1. Transfer procedure: (1) The GCIB (Ar_{3000}^+ 10 keV) is focused on a matrix (blue) reservoir causing its sputtering and redeposition on the sample (orange) surface. (2) An analysis beam, for most experiments Bi_5^+ 30 keV, analyzes the surface modified sample.

by alternating the use of an analysis and a sputter beam, it allows one to perform 3D molecular analysis of the studied sample.[29,30] Alternatively, instruments such as the Ionoptika J105[31] and the recent OrbiSIMS[9] can use a focused continuous beam of large Ar clusters for direct analysis and imaging of biological samples, with comparatively lower lateral resolution (>1 μm) but better molecular/fragment ion ratios. Compared to the small clusters produced in liquid metal ion sources, the low energy per atom (E/n) of the GCIB reduces the damage induced in the sample,[32−34] extending the mass range of biomolecules that can be ionized intact.[35] However, ionization also tends to decrease with decreasing E/n so that ion yields of large biomolecules remain deceptively low, not mentioning the detection schemes, which are not optimized for very large species. Therefore, the mass range is typically limited to 10 kDa (except 12−14 kDa molecules or clusters could be detected[35]), and usually, the biomolecules and pharmaceuticals of interest are in the range 0−1 kDa.[36] Additionally, the condition for the largely submicrometric spatial resolution of SIMS is a very small sputtered volume per pixel which, in combination with an overall low efficiency to produce molecular ions, results in sensitivity issues for a number of biomolecules that happen to be in minute concentration in biological samples.[37]

To enhance SIMS sensitivity and therefore the ability of the technique to detect valuable analytes, researchers focused their work on three approaches: (1) Changing the nature and size of the primary ions. Cluster ions (e.g., Bi_n^+ or C_{60}^+) indeed provided much higher sputtering and secondary ion yields than monoatomic projectiles for organic samples, and moving from large argon to water clusters proved very efficient to increase ionization of biologically relevant molecules, probably via proton transfer from the cluster.[38,39] (2) Postionization right before the entrance of the analyzer, using, for example, lasers, also showed impressive results.[37] (3) As the right sample preparation makes a large difference in the obtained mass spectra,[40−42] several research groups investigated the idea of increasing the acquired signal by cleverly modifying the surface via spraying a thin metallic layer on top of the samples (MetA-SIMS),[43−45] exposing the sample to trifluoroacetic acid or ammoniac vapor[10,46] or depositing an organic acidic MALDI matrix layer (ME-SIMS).[47−50] Recently, an in situ MALDI matrix transfer procedure compatible with 2D and even 3D molecular imaging by SIMS was proposed and tested by the research team of Gilmore[51] and by our team.[52,53] The idea is to take advantage of the low sputtering damage of the 10 keV $Ar_{3000-5000}^+$ ion beam to transfer MALDI matrices, which have shown signal enhancement potential in SIMS, from a reservoir to the sample located next to it (Figure 1). Signal enhancements were observed on different reference biomolecules after the transfer of α-cyano-4-hydroxycinnamic acid, 2,5-dihydroxybenzoic acid, formic acid, as well as 3-nitrobenzonitrile compared to the native sample analysis. The main advantage of this novel approach is that the matrix deposition is performed inside the ultrahigh vacuum chamber of the SIMS instrument. It should therefore cause less analyte delocalization, other solvent or heating-related issues. Importantly, it should also enable 3D analysis with an enhanced signal as there is no need to unload the sample to add a matrix for improved analysis between consecutive sputtering sequences.

The present study aims to clarify the potential of the latter method for lipid detection in tissue samples upon Bi_n^+ and Ar_n^+ bombardment. Six different matrices were compared for a set of samples and analysis conditions. Signal enhancements of intact lipid ions were first determined for reference samples made of an abundant lipid type present in almost any kind of cell membrane, namely phosphatidylcholine (PC). The most promising matrices were then transferred to brain and uterine tissue samples, and the signal enhancement was measured under Bi_5^+ and Ar_{3000}^+ bombardment. The main novelties of this study lie in the analysis of uterine tissue samples, not reported yet to the knowledge of the authors, in the investigation of the matrix-induced sensitivity enhancement of negative ions, and in the comparison of performance of two widespread cluster ion sources for biological sample imaging, Bi_n^+ and Ar_n^+.

2. MATERIALS AND METHODS

2.1. Sample Preparation. Organic compounds such as MALDI matrices and the PC mix reference were purchased from Merck: α-cyano-4-hydroxycinnamic acid (CHCA, 70990), 2,5-dihydroxybenzoic acid (DHB, 85707), sinapinic acid (SA, 85429), 1,5-diaminophthalene (DAN, D21200), 2-mercaptobenzothiazole (MBT, M3302), trihydroxyacetophenone (THAP, 91928) and L-α-Phosphatidylcholine (PC mix, P3556). The substrates for matrix sublimation and for PC mix experiments were 0.3 mm thick [1, 1, 1] square-cut Si wafers (Neyco S.A., Vanves, France). They were cleaned by immersion in a piranha mixture (sulfuric acid/H_2O_2 3:1)

https://doi.org/10.1021/jasms.3c00195
J. Am. Soc. Mass Spectrom. XXXX, XXX, XXX−XXX

followed by ethanol rinsing and drying with a N_2 flow and finally exposed to UV/O_3 treatment for 15 min to remove organic residues from the surface of the substrate.

The matrix reservoirs, also called targets, were manufactured by sublimation in a homemade vacuum apparatus fully described in a previous publication.[52] The temperature/time values for the different matrices were taken from ref 54 and then adjusted (see Table 1) to our sublimation device. The resulting matrix reservoirs are relatively flat and several μm thick.

Table 1. Optimal Sublimation Temperatures/Times for Matrix Reservoir Manufacturing Using a Homemade Sublimation Device

matrix	sublimation temperature (°C)	duration (min)
CHCA	180	120
DHB	130	20
SA	165	10
THAP	130	30
MBT	130	10
DAN	130	20

To produce a relatively flat PC analyte surface, 50 μL of a 5g/L PC mix dissolved in chloroform was spin-coated at 3000 rpm for 30 s.

For the preparation of the mouse brain tissue sections, a cryopreserving protocol was applied in order to prevent the formation of ice crystals, which would break cell membranes and produce holes within the cells. After collection, the mouse brain was immersed in a 4% paraformaldehyde (PFA) solution for 6−18 h at room temperature. Afterward, PFA was replaced with a 10% sucrose solution at 4 °C until the sample sank in the vial. The same operation was repeated with a 30% sucrose solution. The sample was then placed in a plastic mold filled with carboxymethyl cellulose (CMC) that was immersed in isopentane and chilled by liquid nitrogen. CMC is recognized as one of the best embedding media for SIMS analyses, shown to freeze a maximum amount of the different biomolecules.[27] Once the CMC became white and homogeneous, the embedded sample was removed and either conserved in an aluminum foil at −80 °C or directly cut using a cryomicrotome, and the slices were deposited on glass slides. The brain tissue sections had a thickness of about 10 μm and were stored at −20 °C.

Human uterine tissue was obtained as part of a study that received approval from the Ethics Committee of the Université catholique de Louvain (2017/10JUL/362). Tissue samples, collected by biopsy during laparoscopy or following hysterectomy, were provided by the Biobank of Saint-Luc University Clinics as surgical leftovers from patients operated on for clinical reasons independent of the study. Samples were prepared with the same procedure as mouse brain sections and were deposited on indium tin oxide (ITO) glass as recommended in the literature to avoid charge accumulation at the surface of the sample.

2.2. Time of Flight Secondary Ion Mass Spectrometry (ToF-SIMS). Table 2 summarizes the different analyses performed in this work. The main instrument is a TOF.SIMS 5 machine (IONTOF GmbH, Münster, Germany), equipped with both Bi Nanoprobe-LMIG (liquid metal ion gun) and Ar-GCIB (gas cluster ion beam) primary ion sources, providing beams oriented at 45° to the surface normal. For spectral analysis, either a 30 keV Bi_5^+ or a 10 keV Ar_{3000}^+ pulsed ion beam with a cycle time of 200 μs were used to generate secondary ions and a delayed extraction (delay = 1.715 μs) was applied prior to their acceleration toward the analyzer entrance. The primary beam raster areas were set to 500 × 500 and 50 × 50 μm^2 for bismuth and argon analysis, respectively. The measured analysis current was ∼0.5 pA for both ion beams. Each spectral acquisition was repeated 3 times per analyzed sample.

Depth profiling (DP) experiments were conducted by using the dual-beam mode. The 30 keV Bi_5^+ ion beam with a raster of analysis reduced to 200 × 200 μm^2 was used for spectral acquisition while the 10 keV Ar_{3000}^+ with a raster set to 600 × 600 μm^2 was used for sputtering. To avoid the need for charge compensation with the electron gun in the case of sample charging, a pause of 12.44 s was implemented in the analysis cycle. All of the presented DP experiments were at least repeated twice.

For the 2D chemical imaging of the different tissues, the mosaic analysis mode was used. The total area of the tissue slice was divided into 500 × 500 μm^2 squares on which 4 consecutive frames were acquired using the pulsed 30 keV Bi_5^+, 200 μs cycle time, ion beam. A 10 eV electron beam was focused on the sample to resolve sample charging issues when required.

The matrix transfer procedure depicted in Figure 1 was already extensively described in previous publications.[51,52] Briefly, a 10 keV Ar_{3000}^+ ion beam (current = 6 nA) was focused on the matrix reservoir with a 15° impinging angle, and the sample to be analyzed was positioned next to the reservoir in order to collect the sputtered molecules. A matrix layer of about 5−10 nm thickness was transferred to the samples. The layer thicknesses were estimated using the Ar_{3000}^+ ion fluence required to erode the matrix layer and the volumetric sputtering yield was calculated on known matrix

Table 2. Summary of ToF-SIMS Analysis Modes Used for the Acquisition of the Presented Data

method	matrix transfer	analysis modes
in situ ME SIMS on PC references: Figure 2	10 keV Ar_{3000}^+ (2 E16 ions/cm^2)	spectral analysis (30 keV Bi_5^+) and dual beam depth profiling (sput.: 10 keV Ar_{3000}^+)
		positive ion MS
in situ ME SIMS on brain tissues: (a) Figures 3, 4a; Table 3	10 keV Ar_{3000}^+ (2 E16 ions/cm^2)	(a) spectral analysis, 2D mosaic imaging (30 keV Bi_5^+) and dual beam depth profiling (sput.: 10 keV Ar_{3000}^+)
(b) Figure 4b,c		(b) spectral analysis (10 keV Ar_{3000}^+)
		positive ion MS
in situ ME SIMS on uterine tissues: Figure 5; Table 4	10 keV Ar_{3000}^+ (2 E16 ions/cm^2)	spectral analysis, 2D mosaic imaging (30 keV Bi_5^+) and dual beam depth profiling (sput.: 10 keV Ar_{3000}^+)
		positive and negative ion MS

https://doi.org/10.1021/jasms.3c00195
J. Am. Soc. Mass Spectrom. XXXX, XXX, XXX−XXX

a)

Peaks	Mass (Da)	Ion
PC 32:1	732.5	$C_{40}H_{79}NO_8P^+$
PC 32:0	734.5	$C_{40}H_{81}NO_8P^+$
PC 34:2	758.5	$C_{42}H_{81}NO_8P^+$
PC 34:1	760.6	$C_{42}H_{83}NO_8P^+$
PC 36:2	786.6	$C_{44}H_{85}NO_8P^+$
PC 36:1	788.6	$C_{44}H_{87}NO_8P^+$
PC 34:2 + K^+	796.5	$C_{42}H_{80}NO_8PK^+$
PC 36:1 + Na^+	810.6	$C_{44}H_{86}NO_8PNa^+$
PC 38:0 + Na^+	840.6	$C_{46}H_{92}NO_8PNa^+$

b)

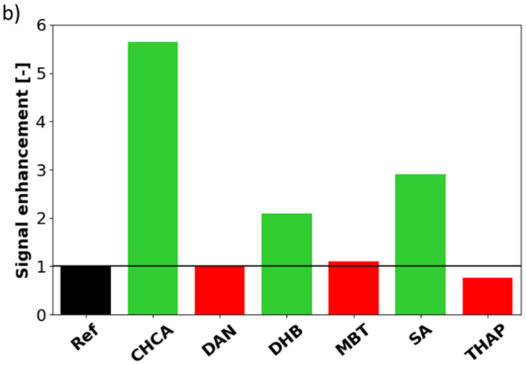

Figure 2. (a) Characteristic ions identified in the PC mix. (b) Average signal enhancement (SE) observed on a PC mix reference sample following the transfer of different MALDI matrices. Acquired signals were normalized by the primary ion doses as well as the normalized signal of the reference. Then the signal enhancement of all 9 identified peaks was averaged. Green indicates matrices for which the SE is significantly greater than 1, i.e., considered potentially useful for further lipid studies.

thickness samples (sputter yield volume of CHCA = 48 ± 5 nm[3][52]). The ion beams were then focused on the surface-modified sample for analysis.

3. RESULTS AND DISCUSSION

3.1. Standard PC Mix Samples. As a preliminary step for the application of the matrix transfer procedure to lipid imaging in biological tissue, the signal enhancement (SE) potential of six MALDI matrices known to be efficient for lipid imaging in MALDI was evaluated (CHCA, DAN, DHB, MBT, SA, and THAP) for a PC mix standard sample. CHCA was previously found to enhance the signal of another PC mix (P2772) by an average factor of 8.9 in a similar experiment.[52] After matrix transfer, the resulting surfaces were depth profiled to evaluate the signal increase through the matrix layer. A reference analysis on the pristine PC layer was also performed. Nine different PC-related peaks could be identified (Figure 2a). Figure 2b presents the average SE observed following matrix transfer for these nine ions. Signals were normalized first by the primary ion dose used for the analysis and by the signal of the pristine PC mix sample. Therefore, a SE value higher than one means increased ion intensity compared to the reference. Then those results were averaged for all 9 peaks to obtain the presented SE values on the figure. It appeared that CHCA (× 5.65 ± 1.5), DHB (× 2.10 ± 0.4), and SA (× 2.91 ± 0.8) are 3 interesting matrices for the detection of PC. The other matrices were thus discarded for the following experiments.

3.2. Mouse Brain Tissue Sections. Given the encouraging results obtained on spin-coated lipid films in section 3.1, mouse brain tissues were the next sample type to be investigated. Reference analyses were performed for comparison with transferred matrix samples and also to make a lipid peak list. The latter (Supplementary Table 1) was made using the abundant literature as well as intuitive combinations to identify lipid derivatives by changing the saturation and fatty acid chain length of known lipids. Only assignments with a deviation of <80 ppm were retained. The promising matrices were thus transferred to brain tissue sections. These were cut in half to facilitate the transfer procedure.

Figure 3a shows the 2D mapping after CHCA transfer. The matrix reservoir was positioned on the left side of the brain slice. The matrix and the white (WM) and gray matter (GM) regions were respectively imaged by the $[M + H]^+$, galactocerebroside (GC) 42:2 $[M + Na]^+$ and PC headgroup

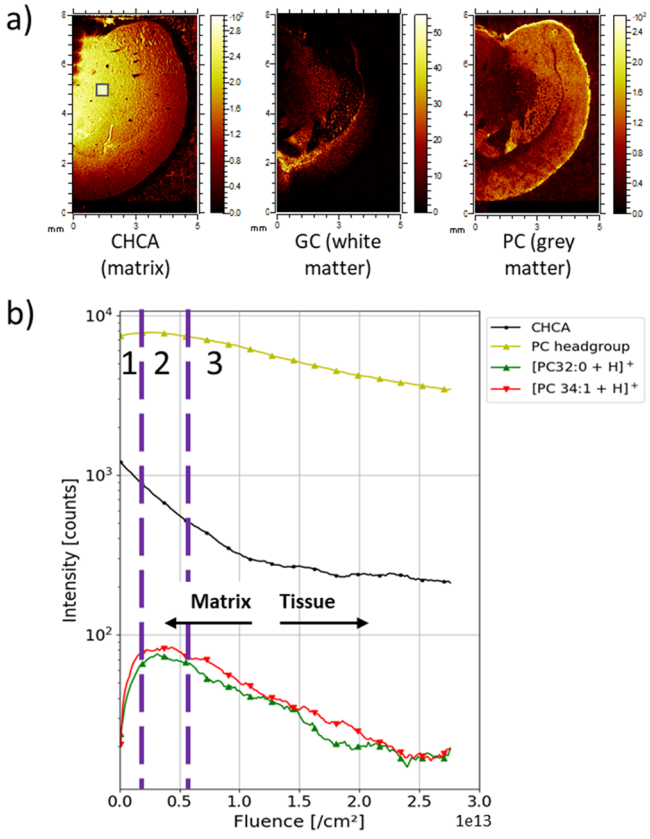

Figure 3. CHCA transfer on a half-mouse brain tissue section. (a) 2D mapping of the half brain post transfer. The matrix reservoir was positioned on the left side of the sample. The matrix $[M + H]^+$ and white (GC 42:1 m/z = 850.62) and gray (PC headgroup, m/z = 184) matter specific signals are depicted from left to right. The depth profiled region of (b) is shown by the gray square on the matrix image. (b) Gray matter depth profiling across the matrix and tissue. The matrix signal is in black, and two PC are depicted in red and green, respectively. Their signal behavior can be divided in 3 zones separated by the purple dashed lines.

$[M + H]^+$. GC is an abundant lipid class located mostly in neuronal tissues (=WM) of animal brains and acting as a structural support for myelin sheets.[55] One can notice that the matrix seems to hide the tissue characteristic peaks on the left side of the cross section that is close to the target. It may suggest that a too thick layer of matrix was deposited on the

https://doi.org/10.1021/jasms.3c00195
J. Am. Soc. Mass Spectrom. XXXX, XXX, XXX−XXX

tissue sample. In order to obtain a more detailed view of the situation, a depth profile was thus performed in this region of the sample to evaluate the SE potential of the 3 selected matrices. The depth profile (Figure 3b), can be divided into 3 zones: in zone 1, at the very surface of the matrix layer, the protonated lipid ion signals are low. In zone 2, inside the matrix layer, the lipid signals appear enhanced compared to zone 3, where only the residual matrix signal remains (there is an interference at that mass with a peak of the tissue) and the lipid intensities level off, indicating that the beam erodes the tissue itself. The depth profile also provides an indication of the matrix layer thickness. Considering a sputter yield volume of 48 nm^3 for CHCA,[52] a fluence of 10^{13} ions/cm^2 should correspond to 5 nm of pure matrix, which is ultrathin compared to the thicknesses needed for MALDI experiments.

Even though the low signal of protonated lipids measured at the beginning of the depth profile seems to indicate that the thickness of the matrix layer prevents diffusion of the molecules of interest to the surface, this explanation does not agree with the high and stable signal of the PC headgroup in the same region and with the very small thickness of the matrix layer. One must therefore suppose that either the protonation of intact molecules is suppressed by a specific chemical environment at the very surface (e.g., high cholesterol concentration) or some surface reactions occurred that damaged the molecules so that the PC headgroup ions remain intense while the parent-like ion is depleted. Comparison with the data of ref 52 confirms that in the case where a pure PC sample was covered by a thicker layer of matrix, both the protonated lipid and the PC headgroup ion intensities decreased in a similar fashion as a function of the distance to the analyte/matrix interface. Therefore, the $[M + H]^+$ depletion at the surface of the matrix layer in Figure 3 is more likely the result of an ion suppression mechanism caused by the surface segregation of other molecules (such as cholesterol). In practice, a solution to avoid any surface effects and obtain the best protonated lipid molecule signal would then be to presputter the surface to analyze with an Ar cluster fluence of around 1.5×10^{12} ions/cm^2.

To evaluate the SE potential, the integrated signal in zone 2 of the depth profiles was compared with a depth profile analysis performed on an untreated mouse brain sample. Once again, the different signal intensities were normalized by the primary ion dose used for analysis. Table 3 shows the SE observed for the transfer of different matrices. All GM and WM lipid rows correspond to an average SE observed for all characteristic high-mass lipid ions identified in each brain zone (Supplementary Table 1): 11, mostly PC, in the gray matter area and 24, mostly GC and PC, in the white matter area. The table also presents the SE for the different kinds of ions: pseudomolecular (+ H^+) and alkaline adduct (+ Na^+ or K^+) ions.

First, the three matrices provide significant signal enhancement for all of the considered GM and WM molecular ion classes, whether they are protonated or cationized by Na or K ions. Among these matrices, CHCA appears to be the best for lipid signal enhancement in both regions of the brain, with an average SE of 6 in the GM and 7 in the WM. It is interesting to note that in the GM region, pseudomolecular ions are slightly more enhanced than alkaline adducts, highlighting the double action of the MALDI matrix on signals mentioned in the literature:[48] (1) it provides a surface structure/chemistry favoring the formation of molecular ions by forming a "nestle environment" for the analyte molecules and (2) it acts as an extra source of protons. Our data show that there is no specific enhancement of the protonated molecules in the WM region and only a slight additional enhancement in the GM region; therefore, the first mechanism seems to play a major role in the measured signal enhancement. The cholesterol signal is strongly enhanced by the presence of the matrix, which is not surprising as it has already been reported that this small lipid tends to diffuse at the surface of biological samples.[56]

Table 3. SE Following Different Matrix Transfers as a Function of the Positive Ion Class for Both Gray and White Matter[a]

brain region	positive ion class	SA	DHB	CHCA
gray matter	cholesterol	25.8	15.0	34.5
	lipid + H	3.8	4.1	6.6
	lipid + Na	2.5	1.9	5.1
	lipid + K	3.0	3.2	5.5
	all GM lipids	**3.3**	**3.3**	**5.9**
white matter	cholesterol	1.6	5.4	11.2
	P inositol	1.3	5.2	16.0
	GC + Na	1.3	2.6	7.4
	GC + K	2.8	3.5	6.1
	PC + H	3.6	3.6	4.3
	PC + Na	2.8	3.7	5.7
	PC + K	2.8	3.7	5.2
	all WM lipids	**2.3**	**3.4**	**7.0**

[a]Signals were normalized by the primary ion dose and the reference signal. Only the brain region characteristic peaks were considered as well as cholesterol ions.

Recent instrumental development of the SIMS primary ion sources made argon cluster ion beams popular in the bioimaging SIMS community.[25,32−34] Therefore, it seemed equally useful to evaluate the matrix enhancement in the case of Ar cluster analysis. However, it is not logistically possible to use the Ar clusters for sputtering and analysis at the same time using our current operating system of the instrument; thus, the SE could not be evaluated by depth profiling. In Figure 3 and previous work, it was shown that the transferred matrix thickness decreases with the distance from the matrix reservoir, following the angular distribution of emission upon transfer.[57] Therefore, the SE properties of DHB and CHCA were evaluated by spectral acquisition using the 10 keV Ar_{3000}^+ beam in delayed extraction mode, at increasing distances from the target as depicted in Figure 4a. On the reference sample, the same peaks were identified as for the Bi cluster analysis, with a slightly better relative intensity.

In Figure 4b, the SE of gray matter characteristic peaks is plotted as a function of the distance from the matrix reservoir. For both DHB and CHCA, the SE increases with the distance until 2.4 mm where it reaches a plateau where the SE is constant until the end of the tissue section (4 mm). It is expected that the acquired signal should decrease to reference intensities at some point but it could not be observed as the size of the tissue section is limited. As for Bi_5^+ analysis, the $[M + H]^+$ ions of high mass characteristic gray matter lipids are enhanced a bit more than the alkaline adducts (Figure 4c). Interestingly, these SE are even larger for Ar than for Bi cluster analysis which is promising regarding the interest of Ar cluster sources in the recent MSI literature. Two additional points should be noted here, in contrast with the Bi_5^+ analysis. First, DHB performs better with Ar_{3000}^+ than Bi_5^+ primary ions and

https://doi.org/10.1021/jasms.3c00195
J. Am. Soc. Mass Spectrom. XXXX, XXX, XXX−XXX

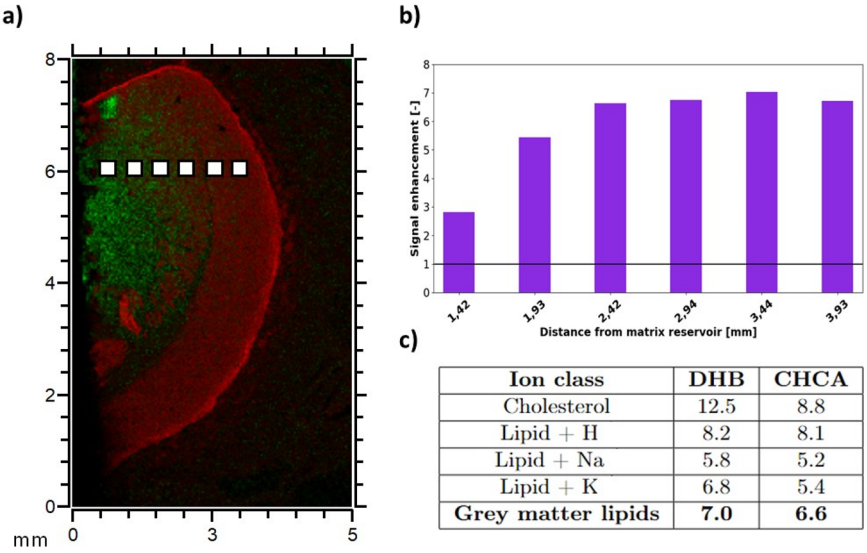

Ion class	DHB	CHCA
Cholesterol	12.5	8.8
Lipid + H	8.2	8.1
Lipid + Na	5.8	5.2
Lipid + K	6.8	5.4
Grey matter lipids	**7.0**	**6.6**

Figure 4. Argon cluster analysis of mouse brain tissue section. (a) 2D mapping of a half brain tissue section following the transfer of CHCA (30 keV Bi_5^+ mosaic imaging). The tissue and the matrix are respectively depicted in red (PC headgroup ion) and green ($C_{10}H_8NO_3^+$ and $C_{10}H_6NO_2^+$). The white squares indicate where Ar cluster analysis spectra were acquired. (b) Average signal enhancement of gray matter specific peaks observed for Ar cluster analysis performed at increasing distance from the CHCA matrix reservoir. (c) SE measured at 2.4 mm for different positive ion classes following the transfer of either DHB or CHCA. Signals were normalized by the primary ion dose and the reference signal.

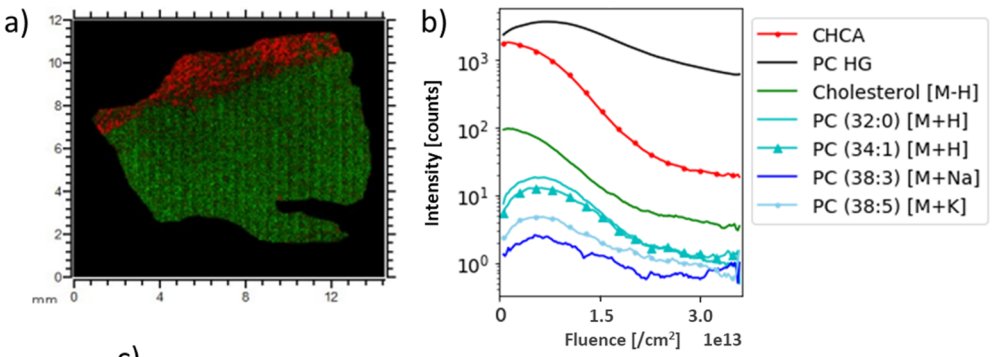

Uterine region	Ion class	DHB	CHCA
Endometrium	Lipid + H	3.4	4.7
	Lipid + Na	2.3	3.4
	Lipid + K	1.8	2.8
	Total	**2.5**	**3.6**
Myometrium	Lipid + H	2.4	8.2
	Lipid + Na	1.7	6.2
	Lipid + K	1.6	4.8
	Total	**1.9**	**6.4**

Figure 5. Uterine tissue section analysis. (a) 2D mapping of an uterine tissue sample by 30 keV Bi_5^+ in the negative polarity; the endometrium and the myometrium tissues are respectively highlighted in red and green. The endometrium is imaged by PI and sulfatide characteristic peaks while the myometrium is imaged by SM and PA characteristic peaks. (b) Depth profile following the transfer of CHCA on a myometrium tissue section in the positive polarity. (c) Averaged SE of lipids in the different tissues following the transfer of DHB and CHCA in the positive polarity.

even slightly better than CHCA. Second, the specific enhancement of the cholesterol signal is much less with Ar_{3000}^+ than Bi_5^+, and it is actually comparable to the enhancement measured for other types of lipids. This might be due to differences between the desorption/ionization mechanisms of these two types of cluster ions.

3.3. Uterine Tissue Sections. Menstrual cycle and diseases affecting the uterus are characterized by changes in the lipid metabolism of the tissues.[58] In the course of a study of hormonal changes during the menstrual cycle and their relation with endometriosis,[59] it was decided to test the matrix transfer protocol on human uterine tissue sections, a biological sample type that has never been studied in MSI to the best of our knowledge. Preliminary reference sample imaging using 30 keV Bi_5^+ primary ions highlighted two different tissues, as shown in Figure 5a: (1) the myometrium, which is a muscular wall that allows the expulsion of the fetus, and (2) the endometrium, which is a dynamic tissue that grows, matures, and is degraded

https://doi.org/10.1021/jasms.3c00195
J. Am. Soc. Mass Spectrom. XXXX, XXX, XXX−XXX

during the menstrual cycle. These regions were identified by a principal component analysis (PCA) run directly with the manufacturer's software. This multivariate analysis was also used to identify the most characteristic peaks of each region, with an emphasis on the intact lipid ions mass range (m/z = 650−900). Prior to PCA analysis, the data were root mean scaled and mean centered.

As no reports of MSI analysis of uterine tissues could be found in the literature, the peaks were putatively annotated by using the formulas of known lipids and accepting a set mass deviation (<80 ppm). The limited mass resolution of ToF instruments leaves a degree of uncertainty to these assignments. These samples should therefore be characterized using an Orbitrap analyzer for unambiguous peak identification.[9,60] With this caveat in mind, a list of 34 peaks with the highly probable assignment was however made in the positive mode and is presented in Supplementary Table 2. Mainly phosphatidylcholine (PC) and sphingomyelin (SM) characteristic peaks were assigned. The myometrium is mostly composed of lighter lipids (5 characteristic peaks), while the endometrium is composed of heavier lipids (13 characteristic peaks). Interestingly, some lipids (16 peaks) were assigned in both regions of the tissue with a difference in relative intensity. The molecular information was also remarkably rich in negative polarity for these uterine tissue sections. Supplementary Figure 1 displays a negative mass spectrum of the endometrium, while Supplementary Figure 2 shows the loadings of the first principal component of the PCA, which clearly separates mass spectra obtained in the myometrium and the endometrium parts of the tissue section. A list of 28 identified peaks is presented in Supplementary Table 3. Here again, the myometrium is characterized by a larger abundance of lighter lipids (10 peaks) such as sphingomyelin (SM, 4 peaks) or phosphatidic acids (PA, 5 peaks) while the endometrium displays higher intensities for heavier lipids (18 peaks) such as phosphatidyl inositol (PI, 9 peaks) or sulfatides (3 peaks). Five peaks were also assigned to phosphatidylethanolamines (PE).

DHB and CHCA were then transferred to both regions of the tissues, and dual beam depth profiles were performed in each zone and in both analyzer polarities (dual beam mode, see Table 2). Figure 5b shows the positive ion depth profile in the myometrium tissue after CHCA transfer. As for the mouse brain samples, the profile can be divided in three zones with the intermediate matrix layer thickness where the highest biomolecular signals are observed. However, at variance with the profile of Figure 3, the PC headgroup signal also decreases going toward the surface in the first zone, which indicates that the matrix layer is too thick for an optimal migration of the lipids at the surface. The table in Figure 5c presents the SE observed for each positive ion type as well as the average enhancement for all lipid characteristic ions. The same data treatment as previously was performed to obtain these SE. CHCA appears once again to be better for lipid detection. Myometrium characteristic ion peaks display higher SE (× 6.4) than those of the endometrium (× 3.6). The obtained SE are slightly lower than those measured for mouse brain samples in the same conditions (see Table 3), but the signals are still significantly larger than those measured for the reference samples.

Finally, the matrix-covered tissue sections were analyzed in the negative polarity because of the very useful negative ion information found for these uterine tissue sections. Table 4 presents the averaged SE observed for lipid characteristic peaks following the transfer of CHCA or DHB. The same data treatment used previously was performed to obtain these SE. It is remarkable that both acidic matrices also lead to intensity enhancements in the negative polarity, although the enhancements vary with respect to those of positive ions in the two parts of the tissue sample. In particular, the matrices favor the enhancement of endometrium more than myometrium negative lipid ions, as opposed to the positive polarity, suggesting a differential ionization effect. Beyond specific ionization effects, one may assume once again that the matrix, extracting the biomolecules from their native tissue location, provides them with a favorable environment for desorption/ionization. In particular, the sputtering yield of the low-molecular weight matrix is larger than the one of tissues made of heavier biomolecules and the diffusing lipids are disentangled from the chemically fixed frozen tissue section. Therefore, the sputtering of intact lipids should be favored and the observed signal increased. The possible emission of biomolecules embedded in matrix clusters might also provide them with a pathway to release energy via matrix molecule evaporation. Other mechanisms involving ion (Na, K) migration in the matrix could also play a role. Comparing the two matrices, CHCA appears once again to be slightly better for lipid detection in the negative polarity.

Table 4. Averaged SE of Lipids in the Different Tissues Following the Transfer of DHB and CHCA in the Negative Polarity

uterine region	ion class	DHB	CHCA
endometrium	PI	3.8	4.2
	sulfatides	4.6	4.9
	PE	2.8	3.6
	all lipids	**3.8**	**4.3**
myometrium	SM	1.5	2.4
	PE	1.9	2.3
	PA	1.8	2.6
	all lipids	**1.7**	**2.5**

4. CONCLUSIONS AND PERSPECTIVES

The recently developed protocol using large Ar cluster ions (GCIB) for in situ matrix transfer was evaluated for different MALDI matrices on increasingly complex samples (lipid mix reference, well-known mouse brain tissue, and human uterine tissue). Two matrices, DHB and CHCA, increase the acquired signal of high-mass lipids in all sample kinds and, more surprisingly, for both secondary ion polarities. The original idea was to benefit from the extra acidic protons and the appropriate molecular "nestle" environment that MALDI matrices bring to the biomolecules for the desorption/ionization process. The results presented here suggest that the second mechanism of signal enhancement is prevalent for intact lipids. Indeed, in the positive polarity, only minor differences in sensitivity enhancements were observed for protonated molecules and alkaline adduct ions. The significant enhancements also measured in the negative ion polarity for uterine tissue samples confirm this interpretation. Therefore, further experiments could explore the signal enhancement potential of other, possibly nonacidic low molecular weight organic or metal−organic molecules.

The bismuth and argon cluster analysis experiments in the presence of CHCA and DHB indicate that 5−10 nm of matrix

https://doi.org/10.1021/jasms.3c00195
J. Am. Soc. Mass Spectrom. XXXX, XXX, XXX−XXX

is sufficient to reach maximum signal enhancement, which is much thinner than that for typical MALDI experiments. In spite of some differences, especially with DHB, the Ar cluster analyses also demonstrate roughly similar enhancements as those obtained with Bi clusters, suggesting that the benefits of in situ ME-SIMS can be generalized to other projectile types. However, optimization of the ion dose used for transfer and of the precise transfer geometry is required for optimal results in direct surface imaging (well controlled and uniform thickness on the whole tissue). Future experiments of in situ matrix enhanced SIMS should therefore focus on two aspects: (1) the optimization of the matrix layer deposition to enable direct 2D imaging of the whole tissue with the maximum enhancement; (2) the investigation of other matrices, not necessarily from the MALDI field but providing optimized molecular extraction and desorption/ionization characteristics under cluster ion impacts.

Finally, by enhancing sensitivity for various classes of lipids, in situ ME SIMS offers a valuable approach for the 2D and 3D high-resolution imaging study of biological tissues affected by diseases modifying their lipidic composition, e.g. Alzheimer's disease,[13] cancer,[61] or endometriosis.[62]

■ ASSOCIATED CONTENT

Supporting Information

The Supporting Information is available free of charge at https://pubs.acs.org/doi/10.1021/jasms.3c00195.

Lists of peak assignments in the SIMS spectra of the brain and uterine tissue cross sections; negative mass spectrum and multivariate analysis loadings graph of the uterine tissue cross sections (PDF)

■ AUTHOR INFORMATION

Corresponding Author

Arnaud Delcorte − *Institute of Condensed Matter and Nanoscience, Université catholique de Louvain, 1348 Louvain-la-Neuve, Belgium;* orcid.org/0000-0003-4127-8650; Email: arnaud.delcorte@uclouvain.be

Authors

Thomas Daphnis − *Institute of Condensed Matter and Nanoscience, Université catholique de Louvain, 1348 Louvain-la-Neuve, Belgium*

Benjamin Tomasetti − *Institute of Condensed Matter and Nanoscience, Université catholique de Louvain, 1348 Louvain-la-Neuve, Belgium*

Vincent Delmez − *Institute of Condensed Matter and Nanoscience, Université catholique de Louvain, 1348 Louvain-la-Neuve, Belgium;* orcid.org/0000-0002-9203-9919

Kevin Vanvarenberg − *Louvain Drug Research Institute, Université catholique de Louvain, 1200 Brussels, Belgium*

Véronique Préat − *Louvain Drug Research Institute, Université catholique de Louvain, 1200 Brussels, Belgium;* orcid.org/0000-0002-4045-1450

Charlotte Thieffry − *Institut De Duve, Université catholique de Louvain, 1200 Brussels, Belgium*

Patrick Henriet − *Institut De Duve, Université catholique de Louvain, 1200 Brussels, Belgium*

Christine Dupont-Gillain − *Institute of Condensed Matter and Nanoscience, Université catholique de Louvain, 1348 Louvain-la-Neuve, Belgium;* orcid.org/0000-0002-6153-4044

Complete contact information is available at: https://pubs.acs.org/10.1021/jasms.3c00195

Notes

The authors declare no competing financial interest.

■ ACKNOWLEDGMENTS

The authors acknowledge the financial support by the Fédération Wallonie Bruxelles, through the project "iBEAM" funded by its research program "Actions de Recherche Concertées" (Convention No. 18/23-090) and by the Belgian National Foundation for Scientific Research (FNRS) through the Research Foundation for Industry and Agriculture (FRIA). B.T. is a research fellow (ASP) of the FNRS. A.D. is a Research Director of the FNRS.

■ REFERENCES

(1) Agüi-Gonzalez, P.; Jähne, S.; Phan, N. T. N. SIMS imaging in neurobiology and cell biology. *J. Anal. At. Spectrom.* **2019**, *34*, 1355−1368.

(2) Noun, M.; Akoumeh, R.; Abbas, I. Cell and tissue imaging by ToF-SIMS and MALDI-TOF: An overview for biological and pharmaceutical Analysis. *Microscopy and Microanalysis* **2022**, *28*, 1−26.

(3) Zhang, J.; Brown, J.; Scurr, D. J.; Bullen, A.; MacLellan-Gibson, K.; Williams, P.; Alexander, M. R.; Hardie, K. R.; Gilmore, I. S.; Rakowska, P. D. Cryo-OrbiSIMS for 3D molecular Imaging of a Bacterial Biofilm in its Native State. *Anal. Chem.* **2020**, *92*, 9008−9015.

(4) Vorng, J.-L.; Kotowska, A. M.; Passarelli, M. K.; West, A.; Marshall, P. S.; Havelund, R.; Seah, M. P.; Dollery, C. T.; Rakowska, P. D.; Gilmore, I. S. Semiempirical Rules To Determine Drug Sensitivity and Ionization Efficiency in Secondary Ion Mass Spectrometry Using a Model Tissue Sample. *Anal. Chem.* **2016**, *88*, 11028−11036.

(5) Passarelli, M. K.; Winograd, N. Lipid imaging with time-of-flight secondary ion mass spectrometry (ToF-SIMS). *Biochimica and biophysica acta* **2011**, *1811*, 976−990.

(6) Scurr, D. J.; Horlacher, T.; Oberli, M. A.; Werz, D. B.; Kroeck, L.; Bufali, S.; Seeberger, P. H.; Shard, A. G.; Alexander, M. R. Surface Characterization of Carbohydrate Microarrays. *Langmuir* **2010**, *26*, 17143−17155.

(7) Edney, M. K.; Kotowska, A. M.; Spanu, M.; Trindade, G. F.; Wilmot, E.; Reid, J.; Barker, J.; Aylott, J. W.; Shard, A. G.; Alexander, M. R.; Snape, C. E.; Scurr, D. J. Molecular formula prediction for chemical filtering of 3D OrbiSIMS Datasets. *Anal. Chem.* **2022**, *94*, 4703−4711.

(8) Sjövall, P.; Lausmaa, J.; Johansson, B. Mass spectrometric imaging of lipids in brain tissue. *Anal. Chem.* **2004**, *76*, 4271−4278.

(9) Passarelli, M. K.; Pirkl, A.; Moellers, R.; Grinfeld, D.; Kollmer, F.; Havelund, R.; Newman, C. F.; Marshall, P. S.; Arlinghaus, H.; Alexander, M. R.; et al. The 3D OrbiSIMS—label-free metabolic imaging with subcellular lateral resolution and high mass-resolving power. *Nat. Methods* **2017**, *14*, 1175−1183.

(10) Angerer, T. B.; Mohammadi, A. S.; Fletcher, J. S. Optimizing sample preparation for anatomical determination in the hippocampus of rodent brain by ToF-SIMS analysis. *Biointerface* **2016**, *11*, No. 02A319.

(11) Körsgen, M.; Pelster, A.; Vens-cappell, S.; Roling, O.; Arlinghaus, H. F. Molecular ME-ToF-SIMS yield as a function of DHB matrix layer thicknesses obtained from brain sections coated by sublimation/deposition technique. *Surf. Interface Anal.* **2016**, *48*, 34−39.

(12) Cersoy, S.; Richardin, P.; Walter, P.; Brunelle, A. Cluster TOF-SIMS imaging of human skin remains: analysis of a South-Andean mummy sample. *Journal of Mass spectrometry* **2012**, *47*, 338−346.

(13) Lazar, A. N.; Bich, C.; Panchal, M.; Desbenoit, N.; Petit, V. W.; Touboul, D.; Dauphinot, L.; Marquer, C.; Laprévote, O.; Brunelle, A.; Duyckaerts, C. Time-of-flight secondary ion mass spectrometry (TOF-SIMS) imaging reveals cholesterol overload in the cerebral cortex of Alzheimer disease patients. *Acta Neuropathologica* **2013**, *125*, 133−144.
(14) Passarelli, M. K.; Newman, C. F.; Marshall, P. S.; West, A.; Gilmore, I. S.; Bunch, J.; Alexander, M. R.; Dollery, C. T. Single-cell analysis: visualizing pharmaceutical and metabolite uptake in cells with label-free 3D mass spectrometry imaging. *Anal. Chem.* **2015**, *87*, 6696−6702.
(15) Nygren, H.; Börner, K.; Hagenhoff, B.; Malmberg, P.; Manson, J. E. Localisation of cholesterol, phosphocholine and galactosylceramide in rat cerebellar cortex with imaging ToF-SIMS equipped with a bismuth cluster ion source. *Biochim. Biophys. acta* **2005**, *1737*, 102−110.
(16) Dumitru, A. C.; Mohammed, D.; Maja, M.; Yang, J.; Verstraeten, S.; del Campo, A.; Mingeot-Leclercq, M.-P.; Tyteca, D.; Alsteens, D. Label-Free Imaging of Cholesterol Assemblies Reveals Hidden Nanomechanics of Breast Cancer Cells. *Adv. Sci.* **2020**, *7*, No. 2002643.
(17) Sämfors, S.; Fletcher, J. S. Lipid diversity in cells and tissue imaging SIMS. *Annu. Rev. Anal. Chem.* **2020**, *13*, 249.
(18) Rohner, T. C.; Staab, D.; Stoeckli, M. MALDI mass spectrometric imaging of biological section. *Mechanisms of Ageing and Development* **2005**, *126*, 177−185.
(19) Sparvero, L. J.; Amoscato, A. A.; Dixon, C. E.; Long, J. B.; Kochanek, P. M.; Pitt, B. R.; Bayir, H.; Kagan, V. E. Mapping of phospholipids by MALDI imaging (MALDI-MSI): realities and expectations. *Chem. Phys. Lipids* **2012**, *165*, 545−562.
(20) He, Q.; Sun, C.; Liu, J.; Pan, Y. MALDI-MSI analysis of cancer drugs: Significance, advances and applications. *Trends in analytical chemistry* **2021**, *136*, No. 116183.
(21) Claude, E.; Jones, E. A.; Pringle, S. D. DESI Mass spectrometry imaging (MSI). *Methods in molecular Biology* **2017**, *1618*, 65−75.
(22) Towers, M. W.; Karancsi, T.; Jones, E. A.; Pringle, S. D.; Claude, E. Optimised Desorption Electrospray Ionisation Mass Spectrometry Imaging (DESI-MSI) for the Analysis of Proteins/Peptides Directly from Tissue Sections on a Travelling Wave Ion Mobility Q-ToF. *J. Am. Soc. Mass Spectrom.* **2018**, *29*, 2456−2466.
(23) He, M. J.; Pu, W.; Wang, X.; Zhang, W.; Tang, D.; Dai, Y. Comparing DESI-MSI and MALDI-MSI Mediated Spatial Metabolomics and Their Applications in Cancer Studies. *Front. Oncol.* **2022**, *12*, No. 891018.
(24) Takats, Z.; Wiseman, J. M.; Gologan, B.; Cooks, R. G. Mass spectrometry sampling under ambient conditions with desorption electrospray ionization. *Science* **2004**, *306*, 471−473.
(25) Ninomiya, S.; Ichiki, K.; Yamada, H.; Nakata, Y.; Seki, T.; Aoki, T.; Matsuo, J. Precise and fast secondary ion mass spectrometry depth profiling of polymer materials with large Ar cluster ion beams. *Rapid commun. Mass Spectrom* **2009**, *23*, 1601−1606.
(26) Kurczy, M. E.; Piehowski, P. D.; Parry, S. A.; Jiang, M.; Chen, G.; Ewing, A. G.; Winograd, N. Which is more important in bioimaging SIMS experiments − the sample preparation or the nature of the projectile. *Appl. Surf. Sci.* **2008**, *255*, 1298−1304.
(27) Yoon, S.; Lee, T. G. Biological tissue sample preparation for time-of-flight secondary ion mass spectrometry (ToF−SIMS) imaging. *Nano convergence* **2018**, *5*, 5−24.
(28) Vickerman, J. C., Briggs, D. *ToF-SIMS: Materials Analysis by Mass Spectrometry*, second ed.; IM Publications, 2013.
(29) Gillen, G.; Fahey, A.; Wagner, M.; Mahoney, C. 3D Molecular Imaging SIMS. *Appl. Surf. Sci.* **2006**, *252*, 6537−6541.
(30) Kassenböhmer, R.; Heeger, M.; Dwivedi, M.; Körsgen, M.; Tyler, B. J.; Galla, H.-J.; Arlinghaus, H. F. 3D Molecular ToF-SIMS Imaging of Artificial Lipid Membranes Using a Discriminant Analysis-Based Algorithm. *Langmuir* **2018**, *34*, 8750−8757.
(31) Fletcher, J. S.; Vickerman, J. C. A new SIMS paradigm for 2D and 3D molecular imaging of bio-systems. *Anal Bioanal. Chem.* **2010**, *396*, 85−104.
(32) Angerer, T. B.; Blenkinsopp, P.; Fletcher, J. S. High energy gas cluster ions for organic and biological analysis by time of flight secondary ion mass spectrometry. *Int. J. Mass Spectrom.* **2015**, *377*, 591−598.
(33) Vanbellingen, Q. P.; Elie, N.; Eller, M. J.; Della-Negra, S.; Touboul, D.; Brunelle, A. Time-of-Flight secondary ion mass spectrometry imaging of biological samples with delayed extraction for high mass and high spatial resolution. *Rapid Commun. Mass Spectrom.* **2015**, *29*, 1187−1195.
(34) Shon, H. K.; Yoon, S.; Moon, J. H.; Lee, T. G. Improved mass resolution and mass accuracy in TOF-SIMS spectra and images using argon gas cluster ion beams. *Biointerphases* **2016**, *11*, 02A321.
(35) Delcorte, A.; Delmez, V.; Dupont-Gillain, Ch.; Lauzin, C.; Jefford, H.; Chundak, M.; Poleunis, C.; Moshkunov, K. Large cluster ions: soft local probes and tools for organic and bio surfaces. *Phys. Chem. Chem. Phys.* **2020**, *22*, 17427−17447.
(36) Mochiji, K.; Hashinokuchi, M.; Moritani, K.; Toyoda, N. Matrix-free detection of intact ions from proteins in argon-cluster secondary ion mass spectrometry. *Rapid Commun. Mass Spectrom.* **2009**, *23*, 648−652.
(37) Gilmore, I. S.; Heiles, S.; Pieterse, C. L. Metabolic Imaging at the Single-Cell Scale: Recent Advances in Mass Spectrometry Imaging. *Annu. Rev. Anal. Chem.* **2019**, *12*, 201−224.
(38) Berrueta Razo, I.; Sheraz, S.; Henderson, A.; Lockyer, N. P.; Vickerman, J. C. Mass spectrometric imaging of brain tissue by time-of-flight secondary ion mass spectrometry − How do polyatomic primary beams C60+, Ar2000+, water-doped Ar2000+ and (H2O)-6000+ compare? *Rapid Commun. Mass Spectrom.* **2015**, *29*, 1851−1862.
(39) Dimovska Nilsson, K.; Karagianni, A.; Kaya, I.; Henricsson, M.; Fletcher, J. S. (CO2)n+, (H2O)n+, and (H2O)n+(CO2) gas cluster ion beam secondary ion mass spectrometry: analysis of lipid extracts, cells and Alzheimer's model mouse brain tissue. *Anal. and Bioanal. Chem.* **2021**, *413*, 4181−4194.
(40) Malm, J.; Giannaras, D.; Riehle, M. O.; Gadegaard, N.; Sjövall, P. Fixation and drying protocols for the preparation of cell samples for Time-of-Flight Secondary Ion Mass Spectrometry analysis. *Anal. Chem.* **2009**, *81*, 7197−7205.
(41) Flinders, B.; Cuypers, E.; Zeijlemaker, H.; Tytgat, J.; Heeren, R. M. A. Preparation of longitudinal sections of hair samples for the analysis of cocaine by MALDI-MS/MS and ToF-SIMS imaging. *Drug Test. Analysis* **2015**, *7*, 859−865.
(42) Dong, Y.; Li, B.; Malitsky, S.; Rogachev, I.; Aharoni, A.; Kaftan, F.; Svatos, A.; Franceschi, P. Sample preparation of mass spectrometry imaging of plant tissues, a review. *Frontiers in Plant Science* **2016**, *7*, 60.
(43) Altelaar, A. F. M.; Piersma, S. R. Cellular Imaging Using Matrix-Enhanced and Metal-Assisted SIMS. *Methods Mol. Biol.* **2010**, *656*, 197−208.
(44) Delcorte, A.; Médard, N.; Bertrand, P. Organic Secondary Ion Mass Spectrometry: Sensitivity Enhancement by Gold Deposition. *Anal. Chem.* **2002**, *74*, 4955−4968.
(45) Yamazaki, A.; Tobe, T.; Akiba, S.; Owari, M. Metal-assisted SIMS for three-dimensional analysis using shave-off section processing. *Surf. Interface Anal.* **2014**, *46*, 1215−1218.
(46) Angerer, T. B.; Dowlatshahi Pour, M.; Malmberg, P.; Fletcher, J. S. Improved molecular imaging in rodent brain with time-of-flight secondary ion mass spectrometry using gas cluster ion beams and reactive vapour exposure. *Anal. Chem.* **2015**, *87*, 4305−4313.
(47) Svara, F. N.; Kiss, A.; Jaskolla, T. W.; Karas, M.; Heeren, R. M. A. High-Reactivity matrices increase the sensitivity of Matrix Enhanced Secondary ion mass spectrometry. *Anal. Chem.* **2011**, *83*, 8308−8313.
(48) Jones, E. A.; Lockyer, N. P.; Kordys, J.; Vickerman, J. C. Suppression and Enhancement of secondary ion formation due to the chemical environment in static-secondary ion mass spectrometry. *J. Am. Soc. Mass Spectrom.* **2007**, *18*, 1559−1567.
(49) Locklear, J. E.; Guillermier, C.; Verkhoturov, S. V.; Schweikert, E. A. Matrix enhanced cluster-SIMS. *Appl. Surf. Sci.* **2006**, *252*, 6624−6627.

https://doi.org/10.1021/jasms.3c00195
J. Am. Soc. Mass Spectrom. XXXX, XXX, XXX−XXX

(50) Dowlatshahi Pour, M.; Malmberg, P.; Ewing, A. An investigation on the mechanism of sublimated DHB matrix on molecular ion yiels in SIMS imaging of brain tissue. *Anal. Bioanal. Chem.* **2016**, *408*, 3071−3081.
(51) Lorenz, M.; Zhang, J.; Shard, A. G.; Vorng, J.-L.; Rakowska, P. D.; Gilmore, I. S. Method for molecular layer deposition using gas cluster ion beam sputtering with example application In Situ matrix enhanced secondary ion mass spectrometry. *Anal. Chem.* **2021**, *93*, 3436−3444.
(52) Moshkunov, K.; Tomasetti, B.; Daphnis, Th.; Delmez, V.; Vanvarenberg, K.; Préat, V.; Lorenz, M.; Quanico, J.; Baggerman, G.; Lemiere, F.; Dupont, C.; Delcorte, A. Improvement of biomolecular analysis in thin films using in situ matrix enhanced secondary ion mass spectrometry. *Analyst* **2021**, *146*, 6506−6519.
(53) Delmez, V.; Degand, H.; Poleunis, C.; Moshkunov, K.; Chundak, M.; Dupont-Gillain, C.; Delcorte, A. Deposition of Intact and Active Proteins In Vacuo Using Large Argon Cluster Ion Beams. *J. Phys. Chem. Lett.* **2021**, *12*, 952−957.
(54) Thomas, A.; Charbonneau, J. L.; Fournaise, E.; Chaurand, P. Sublimation of New Matrix Candidates for High Spatial Resolution Imaging Mass Spectrometry of Lipids: Enhanced Information in Both Positive and Negative Polarities after 1,5-Diaminonapthalene Deposition. *J. Am. Chem. Soc.* **2012**, *84*, 2048−2054.
(55) Baba, H., Ishibashi, T. The Role of Sulfatides in Axon-Glia Interactions. In *Myelyn, Basic and Clinical Advances*; Springer, 2019; pp 165−179.
(56) Sjövall, P.; Johansson, B.; Lausmaa, J. Localization of lipids in freeze-dried mouse brain sections by imaging TOF-SIMS. *Appl. Surf. Sci.* **2006**, *252*, 6966−6974.
(57) Delmez, V.; Tomasetti, B.; Daphnis, Th.; Poleunis, C.; Lauzin, C.; Dupont-Gillain, Ch.; Delcorte, A. Gas Cluster Ion Beams as a Versatile Soft-Landing Tool for the Controlled Construction of Thin (Bio) Films. *Applied bio mater* **2022**, *5*, 3180−3192.
(58) Peinado, F. M.; Olivas-Martínez, A.; Iribarne-Durán, L. M.; Ubiña, A.; León, J.; Vela-Soria, F.; Fernández-Parra, J.; Fernández, M. F.; Olea, N.; Freire, C.; Ocón-Hernández, O.; Artacho-Cordón, F. Cell cycle, apoptosis, cell differentiation, and lipid metabolism gene expression in endometriotic tissue and exposure to parabens and benzophenones. *Sci. Total Environ.* **2023**, *879*, No. 163014.
(59) Thieffry, C.; Van Wynendaele, M.; Samain, L.; Tyteca, D.; Pierreux, C.; Marbaix, E.; Henriet, P. Spatiotemporal expression pattern of Progesterone Receptor Component (PGRMC) 1 in endometrium from patients with or without endometriosis or adenomyosis. *Journal of Steroid Biochemistry and Molecular Biology* **2022**, *223*, No. 106153.
(60) Kotowska, A. M.; Trindade, G. F.; Mendes, P. M.; Williams, P. M.; Aylott, J. W.; Shard, A. G.; Alexander, M. R.; Scurr, D. J. Protein identification by 3D OrbiSIMS to facilitate in situ imaging and depth profiling. *Nat. Commun.* **2020**, *11*, 1−8.
(61) Vasseur, S.; Guillaumond, F. Lipids in cancer: a global view of the contribution of lipid pathways to metastatic formation and treatment resistance. *Oncogenesis* **2022**, *11*, 46.
(62) Chagovets, V. V.; Wang, Z.; Kononikhin, A. S.; Starodubtseva, N. L.; Borisova, A.; Salimova, D.; Popov, I. A.; Kozachenko, A. V.; Chingin, K.; Chen, H.; Frankevich, V. E.; Adamyan, L. V.; Sukhikh, G. T. Endometriosis foci differentiation by rapid lipid profiling using tissue spray ionization and high resolution mass spectrometry. *Sci. Rep.* **2017**, *7*, 2546.

https://doi.org/10.1021/jasms.3c00195
J. Am. Soc. Mass Spectrom. XXXX, XXX, XXX−XXX